Design of Piezoelectric Micromachined Ultrasonic Transducers Using High-Order Mode With High Performance and High Frequency

KANGFU LIU [1,2,3] **(Student Member, IEEE), YAOQING LU** [1,2,3] **(Student Member, IEEE), SHENG WU** [1,2,3] **(Student Member, IEEE), XINXIN LI** [1,2,3], **AND TAO WU** [1,2,3,4] **(Senior Member, IEEE)**

[1] School of Information Science and Technology, ShanghaiTech University, Shanghai 201210, China
[2] Shanghai Institute of Microsystem and Information Technology, Chinese Academy of Sciences, Shanghai 200050, China
[3] University of Chinese Academy of Sciences, Beijing 100049, China
[4] Shanghai Engineering Research Center of Energy Efficient and Custom AI IC, Shanghai 201210, China
CORRESPONDING AUTHOR: T. WU (wutao@shanghaitech.edu.cn)

ABSTRACT This work proposes the piezoelectric micromachined ultrasonic transducer (pMUT) design using high-order mode. Analytical models are established and used to estimate the performance of pMUT in n^{th}-order axisymmetric mode. To prove the concept, a comprehensive analysis is conducted on the 3rd-order pMUT by finite element method (FEM). The analytical models give guidance for the design of electrode configuration and geometric dimensions, which are verified by FEM. With optimized electrode configuration and thickness, the proposed pMUT design shows extraordinary performance improvement in transmitting and round-trip sensitivity. Approximately $10.2\times$ and $4.12\times$ improvements in transmitting sensitivity and round-trip sensitivity have been achieved compared to the traditional 1st-order pMUT in the same radius, while there is an $8.6\times$ improvement of the receiving voltage in the pulse-echo analysis. The high frequency, round-trip sensitivity, and directivity features of the proposed high-order pMUT design shown in FEM make it very promising for forming a high-frequency large-scale pMUT array.

INDEX TERMS High frequency, high order mode, piezoelectric micromachined ultrasonic transducers (PMUTs), high sensitivity, directivity.

I. INTRODUCTION

PIEZOELECTRIC micromachined ultrasonic transducers (pMUTs) ultrasonic transducers have been used in the application of fingerprint recognition, object detection, and particularly medical imaging [1], [2]. Conventional ultrasonic transducers based on bulk piezoelectric ceramic have poor acoustic coupling to air or liquid, and it is expensive to machine them into a two-dimensional (2D) transducer array for three-dimensional (3D) imaging. Instead, the micromachined ultrasonic transducer has a low acoustic impedance for good coupling to air/liquids. Furthermore, pMUTs have the advantages of small element size, low power consumption, low cost, and easy integration with supporting electronics [3].

The pMUTs with both high transmission and receiving sensitivity are needed for a high signal-to-noise ratio (SNR) detection. The designs with bimorph layers [4], curved shape [5], and Helmholtz resonant cavity [6] are proposed to improve the transmitting performance. However, the bimorph design leads to complex interconnection, and design with a curved shape, Helmholtz tube, or cavity requires additional processes. Furthermore, these works focus on the transmitting performance and neglect the receiving performance.

High-frequency ($\geq$ 10 MHz) pMUT is an attractive option to substitute bulk piezoelectric transducer for arrays without expensive dicing process [2]. Higher frequency represents higher spatial resolution but higher attenuation in the medium, which would be able to apply in applications

that required high resolution in a short distance, such as fingerprint recognition and endoscopic imaging. Previous pMUT studies mainly focus on fundamental mode, Smith [7], [8] gives the analytical solution of Green's function and equivalent circuit model for multi-ring electrode actuated pMUT, but did not give the optimal electrode design rules for high-order mode. Multivariate optimization is difficult, even impractical. Furthermore, the superiorities of high-order modes in transmitting and round-trip performance have not been revealed yet.

This work proposes pMUT designs using the higher-order mode and proves the superiorities of high-order modes in transmitting sensitivity, round-trip sensitivity, and directivity. Analytical models are established for high-order pMUTs, which are verified by finite element method (FEM) simulations. The simple analytical solution of the stress nodal point guides the electrode design for high-order modes. The round-trip sensitivity-bandwidth product is adopted for the optimization metric rather than a single metric of displacement, coupling coefficient, or transmitting pressure, which gives widely applicable and stabilized guidance for thickness optimization. To prove the concept of high-order mode, the 3rd-order mode pMUT is selected as an example. With the optimizations of electrode and thickness, the 3rd-order mode optimized pMUT demonstrates significant improvements compared to 1st-order mode optimized pMUT in terms of transmitting sensitivity, round-trip sensitivity, and directivity.

II. THEORY FOR HIGH-ORDER pMUT
A. MODE SHAPE AND RESONANT FREQUENCY
A pMUT device with an unimorph structure including stack layers of electrodes, piezoelectric material, and supporting material could be approximated as a uniform thin plate with clamped boundary. A multi-electrodes actuated circular plate consisting of multi-layers with clamped boundaries will be analyzed in the following, the cross-section view and the top view of the plate are shown as Figs. 1 (a) and 1(b), respectively. Where h_i and z_i are the height of the top plane and midplane of i-th layer, respectively; r_j' and r_j'' are the inner and outer radius for j-th electrode. For the homogeneous clamped circular plate with a radius of a, the deflection function w can be expressed in the following form [9]:

$$w(\overline{r}, \theta, t) = \sum_{m=0}^{\infty} \sum_{n=0}^{\infty} A_{mn} \psi_{mn}(\overline{r}) \cos(m\theta) \sin(\omega t) \quad \text{(1a)}$$

$$\psi_{mn}(\overline{r}) = J_m(\lambda_{mn}\overline{r}) - \frac{J_m(\lambda_{mn})}{I_m(\lambda_{mn})} I_m(\lambda_{mn}\overline{r}) \quad \text{(1b)}$$

where m refers to the number of nodal diameters and n represents the number of nodal circles including the boundary circle. For the sake of simplicity, the mode shape with m nodal diameters and n nodal circles is referred to as (m, n). $\overline{r} = r/a$ is the normalized radial coordinate, and θ is the angle coordinate. A_{mn} is the displacement amplitude of corresponding mode shape, and ψ_{mn} is the eigenfunction of

TABLE 1. Normalized radius of stress nodal circle, when $m = 0$, $\nu = 0.3$.

n	1	2	3	4	5
$\overline{r}$	0.677	0.39	0.257	0.192, 0.440	0.153, 0.352
		0.84	0.591	0.692, 0.919	0.552, 0.753
			0.893		0.935

the mode shape profile. J_m and I_m are the Bessel function and the modified Bessel function of the first kind. The mode shape constant λ_{mn} is determined by boundaries, and its value is given by [9].

In the previous study, the first axisymmetric mode $(0, 1)$ of pMUT is considered to possess the maximum volumetric displacement and velocity, thus producing the highest possible acoustic pressure [7]. However, the resonant frequency of the third axisymmetric mode $(0, 3)$ is more than 10 times of mode $(0, 1)$, resulting in a higher acoustic pressure, since the output pressure of pMUT is proportional to ω^2. In the following discussion, the non-axisymmetric modes $(m \neq 0)$ are neglected to simplify the derivation.

To excite the modes effectively, the gap of electrodes should be placed and aligned with the nodal circle of volumetric stress. Solve equation of motion [9] with a boundary of $\nabla^2 w|_{\overline{r}=1} = 0$, the nodal circle radius can be obtained from the root of the equation:

$$J_0(\lambda\overline{r}) = \frac{(1-\nu)\lambda J_0'(\lambda) + \lambda^2 J_0(\lambda)}{(1-\nu)\lambda \frac{I_0'(\lambda)}{I_0(\lambda\overline{r})} - \lambda^2 \frac{I_0(\lambda)}{I_0(\lambda\overline{r})}} \quad \text{(2)}$$

where ν is the Poisson ratio. Table 1 summaries the roots of (2) for the first five axisymmetric modes, when $\nu = 0.3$. For instance, the nodal circle of mode $(0, 1)$ is located at $\overline{r} = 0.677$. This result is consistent with the fact that most of the conventional pMUT designs [3], [10] optimize the electrode coverage to 70% for maximum displacement. The slight difference is due to the adoption of the deflection function approximation $(1 - \overline{r}^2)^2$ used in these studies. For mode $(0, 3)$ with $\nu = 0.3$, the nodal circle is located at $\overline{r} = \{0.256, 0.591, 0.893\}$. The solution of the stress nodal circle gives guidance for the optimal electrode design.

The natural frequencies of the circular plate in a vacuum are expressed as:

$$\omega_{0n,V} = \frac{\lambda^2}{a^2} \sqrt{\frac{D}{\mu}} \quad \text{(3)}$$

where D is the flexure rigidity of the plate and μ is the mass per area. The rigidity D and mass per area μ of the stack layers are calculated as [11].

Assume that the mode shape is the same in vacuum and water. For the application with one side of pMUT contact with liquid, the natural frequencies can be evaluated by [12]:

$$\omega_{0n,L} = \frac{\omega_{0n,V}}{\sqrt{1 + \beta_{0n}}}, \quad \beta_{0n} = \Gamma_{0n} \frac{\rho_0 a}{\mu} \quad \text{(4)}$$
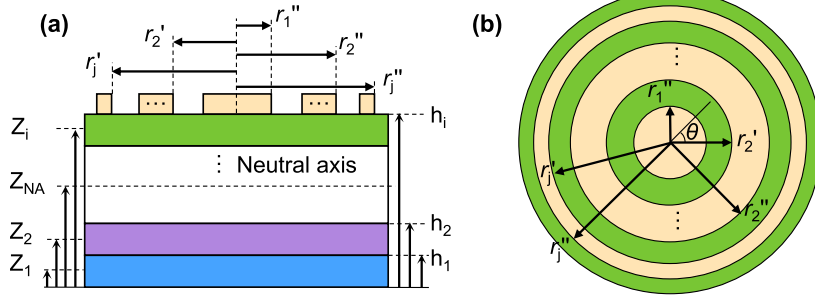
FIGURE 1. (a) Cross-section view and (b) top view of the multi-electrodes actuated circular plate consist of multi-layers with clamped boundary.

where β_{0n} is the added virtual mass incremental factor, which represents the kinetic energy ratio of the liquid to the plate. Γ_{0n} is a nondimensional added virtual mass incremental factor and its numerical solution in water is given by [13].

B. TRANSMITTING SENSITIVITY

For transmission, the sound pressure output in far-field at a distance l is revised from [14]:

$$p_{tx}(r, \theta) = \frac{R_0 P_0}{l} D(\theta) \approx \frac{\rho_0 a^2 \omega^2 u_{av}}{2l} D(\theta) \qquad (5)$$

where $R_0 = ka^2/2$ is the Rayleigh distance; $k = \omega/c_0$ is the wave number in loaded medium. The surface pressure is $P_0 = \rho_0 c_0 \omega u_{av}$. ρ_0 and c_0 are the density and acoustic speed of the medium. The amplitude directivity factor $D(\theta)$ is defined as the pressure at angle θ relative to that at $\theta = 0$. The average displacement amplitude u_{av} of mode $(0, n)$ is given by:

$$u_{av} = \frac{\int_0^a \psi(r) 2\pi r \, dr}{\pi a^2} = \sum_n A_{0n} \alpha_{0n} \qquad (6a)$$

$$\alpha_{0n} = 2 \int_0^1 \psi_{0n}(\bar{r}) \bar{r} \, d\bar{r} \qquad (6b)$$

where α_{0n} represents the effective factor of mode $(0, n)$ to a uniform piston disk with the same radius. The α_{0n} for the first five axisymmetric modes are {0.3291, -0.1309, 0.0736, -0.0486, 0.03506}. The effective factors for even-order axisymmetric modes are negative, indicating the acoustic wave is emitted in a negative direction, resulting in the valleys of the transmitting response, while odd-order modes emit in a positive direction and produce peaks.

The displacement amplitude A_{0n} should be Q times of static displacement, i.e., $A_{0n} = A_0 Q_{0n}$, where Q_{0n} is the corresponding quality factor of mode $(0, n)$; A_0 is the static displacement and is given by [15] and [16]:

$$A_0 = a^2 \frac{M_p I_p}{D I_D} = a^2 \frac{|e_{31,f}| z_p V_{in} I_p}{D I_D} = A_s V_{in} \qquad (7)$$

$$A_s = a^2 \frac{|e_{31,f}| z_p I_p}{D I_D} \qquad (8)$$

$$e_{31,f} = \frac{d_{31}}{s_{11} + s_{12}} = e_{31} - \frac{c_{13}}{c_{33}} e_{33} \qquad (9)$$

TABLE 2. Non-dimensional parameters for circular clamped plate, when $m = 0$.

n	1	2	3	4	5
λ	3.195474	6.306424	9.439501	12.57713	15.71644
α_{0n}	0.329119	-0.13093	0.073633	-0.04856	0.035059
$I_{p,max}$	12.43940	33.51852	61.33494	94.39001	131.9422
I_D	66.71717	503.7789	1685.102	3982.684	7768.577
Γ_{0n}	0.653957	0.276129	0.165127	0.115410	0.087860

where A_s is the static displacement sensitivity (in a unit of m/V). M_p is the bending moment produced by the piezoelectric layer. z_p is the distance between the mid-plane of the piezoelectric layer and the neutral axis. Equation (9) shows that the piezoelectric coefficient involved in the generation of bending moment includes both e_{31} and e_{33}.

I_D and I_p in (7) are integrals related to the elastic energy and coupled energy between the electric domain and mechanic domain [17]. Neglecting the Poisson ratio ν related terms, I_D is a constant for specific mode shape. The value of I_D can be obtained by numerical integration. I_p is an integral related to the electrode configuration. The maximum value of I_p can be obtained by alternately applying voltages of opposite polarities separated by zeros of the integrand. With the ideal full coverage optimal electrode ($r_j'' = r_{j+1}'$), the maximum value of I_p is:

$$I_{p,max} = \int_0^1 \left| \frac{d^2 \psi_{0n}}{dr^2} + \frac{1}{r} \frac{d\psi_{0n}}{dr} \right| 2\pi r \, dr \qquad (10)$$

Table 2 lists the non-dimensional parameters which are necessary for the calculation of sound pressure for the first five axisymmetric modes ($m = 0$) in the circular clamped plate immersed in water.

Combine (5)-(9), the relationship between output pressure and the key parameters can be obtained:

$$S_{\text{Tx}} = \left| \frac{p_{tx}}{V_{in}} \right| \propto a^2 \omega_{0n,L}^2 \cdot A_s \alpha_{0n} Q_{0n}$$

$$\propto \alpha_{0n} \lambda_{0n}^4 \cdot \frac{I_p}{I_D} \cdot \frac{1}{1 + \beta_{0n}} \cdot |e_{31,f}| \cdot \frac{z_p}{\mu} \cdot Q_{0n} \qquad (11)$$

where α_{0n} and λ_{0n} are the mode shape relevant constants and are positively related to n, which help the high-order

modes achieve higher $\omega_{0n,L}$ and S_{Tx}. I_p/I_D is determined by the electrode design, the maximum value $I_{p,max}/I_D$ of which corresponds to the optimal electrode configuration. $1/(1+\beta_{0n})$ represents the descent of resonant frequency of the plate when it is in contact with water compared with that when it is in the vacuum. The $|e_{31,f}|$ term shows that the piezoelectric material with high $|e_{31,f}|$ are preferred. z_p/μ is related to the thicknesses of stack layers.

When the material properties of pMUT and acoustic medium are given, the normalized transmitting sensitivity for n^{th}-order mode can be obtained. For instance, neglect difference of $|e_{31,f}|$, z_p and Q, given $a = 50$ µm, $\mu = 8.4$ mg/m^2, $\rho_0 = 1000$ kg/m^3, the normalized transmitting sensitivity for 1st, 3rd, 5th modes are {1, 8.2, 18.2}, respectively. This result illustrates the remarkable improvement of emission performance for high-order mode compared with fundamental mode.

The Q-factor is difficult to parse with a single formula. There are multiple sources of loss:

$$\frac{1}{Q} = \frac{1}{Q_{rad}} + \frac{1}{Q_{support}} + \frac{1}{Q_{TED}} + \frac{1}{Q_{other}} \qquad (12)$$

where $1/Q_{rad}$ is due to the energy radiated to the loaded medium; $Q_{rad} \propto 1/\sqrt{v/(\omega a^2)}$ [18]; v is kinematic viscosity, for water, $v = 1.14 \times 10^{-6}$ m^{2}s^{-1}. $1/Q_{support}$ is the support loss, and $Q_{support} \propto (a/t)^3$ [19]. $1/Q_{TED}$ is the thermoelastic damping, and $1/Q_{other}$ represents the other intrinsic losses.

C. RECEIVING SENSITIVITY

The elastic energy U_D and coupled energy U_p of thin plate can be associated with displacement [11]:

$$U_D = \frac{1}{2}\frac{D}{a^2}I_D u_{0,rx}^2 \qquad (13a)$$

$$U_p = \frac{1}{2}M_p I_p u_{0,rx} \qquad (13b)$$

where $u_{0,rx}^2$ is the displacement amplitude in the reception. Neglecting the loses and assuming that the work U_s of sound waves act on the film is converted completely to the elastic energy U_D, and the piezoelectric energy U_p is thoroughly converted to electrical energy U_e, the following equations can be derived:

$$U_D = U_s = p_{in}S \cdot u_{0,rx} \qquad (14a)$$

$$U_p = U_e = \frac{1}{2}C_0 V_{out}^2 \qquad (14b)$$

where S is the cavity area of pMUT; C_0 is the device static capacitance, and $u_{0,rx}^2$ is the displacement amplitude in reception. Then the pMUT receiving sensitivity can be derived as:

$$S_{Rx} = \left|\frac{V_{out}}{p_{in}}\right| = A_s \alpha_{0n} Q_{0n} \cdot \frac{2S}{C_0} \qquad (15)$$

where A_s is the static displacement sensitivity; S is the cavity area of pMUT, C_0 is the device static capacitance. Thus, the

devices with high displacement sensitivity are preferred in the receiving. With n increases, the effective displacement factor α_{0n} decreases, leading to the disadvantage of high-order modes ($n > 1$) in receiving sensitivity.

D. SENSITIVITY-BANDWIDTH PRODUCT

The sensitivity-bandwidth (SBW) product is given by:

$$\text{SBW}_x = \max(S_x) \cdot \text{FBW}_x \qquad (16)$$

where S_x is sensitivity, x can be replaced with Tx, Rx, and RT, representing the transmitting, receiving, and round-trip performance, respectively. Particularly, FBW is -6 dB fractional bandwidth for round-trip sensitivity.

The round-trip sensitivity is defined as $S_{RT} = S_{Tx} \cdot S_{Rx}$. The round-trip sensitivity bandwidth product SBW_{RT} is adopted as the optimization criterion in this work rather than a single parameter of displacement [20], sound pressure level [21] and electromechanical coupling coefficient [17], since it represents the global transmitting-receiving sensitivity and bandwidth in loaded condition, which consider the process from excitation to reception. Besides, the sensitivity and bandwidth (FBW $\approx 1/Q$) are mutually compromising factors, thus making SBW a widely applicable and relatively stabilized coefficient [22]. Combine (11), (15) and (16), with the same cavity radius, the dependency of SBW_{RT} with resonant frequency f_0 and displacement sensitivity A_s are:

$$\text{SBW}_{RT} \propto (f_0 A_s)^2 \qquad (17)$$

The round-trip performance is fundamentally determined by the product of resonant frequency and displacement sensitivity.

E. DIRECTIVITY

Directivity indicates the spatial distribution of radiant energy. High directivity raises the signal level and decreases the noise level in non-target directions. The radiation pattern product theorem [14] shows that the directivity of the pMUT array is equal to the product of the array factor and the element. Thus, high-directional pMUT elements are conducive to forming high-directional arrays. The normalized directivity of mode $(0, n)$ is given by:

$$D_{0n}(\theta) = \frac{\int_0^1 \psi_{0n}(r)J_0(ka\sin(\theta)r)r\,dr}{\int_0^1 \psi_{0n}(r)r\,dr} \qquad (18)$$

III. OPTIMIZATION

To prove the concept and validate the superiority of the proposed high-order pMUT, mode $(0, 3)$ is selected as an example for the following analysis considering the trade-off between the transmitting and receiving sensitivity. The electrode design and geometric optimization will be discussed.

A. SETUP OF FEM MODELS

To evaluate the proposed high-order pMUT design, 2D axisymmetric FEM models are set up in COMSOL
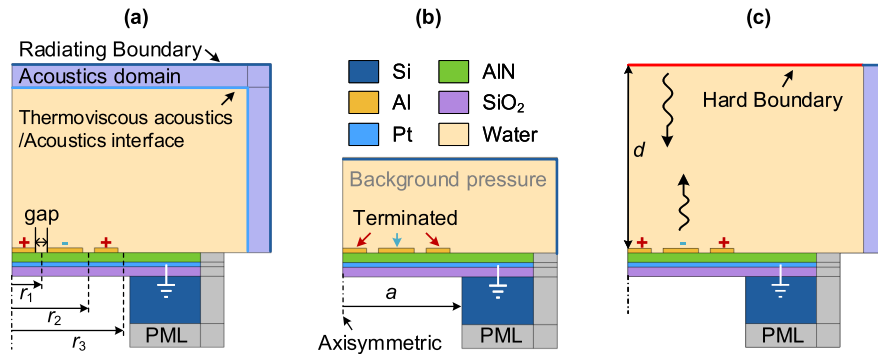
FIGURE 2. The configuration of 2D axisymmetric FEM models of pMUT for (a) transmitting sensitivity (b) receiving sensitivity and (c) pulse-echo response.

TABLE 3. Summary of the initial geometry parameters.

Symbol	Value	Unit	Description
t_{TE}	0.2	μm	Top electrode thickness
t_p	0.75	μm	Piezoelectric layer thickness
t_{BE}	0.1	μm	Bottom electrode thickness
t_{ox}	2	μm	Passive layer thickness
a	50	μm	Cavity radius
gap	0.05	-	Normalized gap
r_1	0.257		
r_2	0.591	-	Normalized radius
r_3	0.893		

Multiphysics. Default material parameters in COMSOL are adopted. Figs. 2 (a)-(c) show the configuration of COMSOL models for simulating transmitting sensitivity, receiving sensitivity, and pulse-echo response, respectively. The geometries are not shown in proportion, in order to illustrate setups. Table 3 summarizes the initial geometry parameters. The sensitivity simulations in the frequency domain give the full band information and optimization guidance which is more stable and efficient, while the pulse-echo simulation in the time domain gives the round-trip performance including the transmitting and receiving process, which evaluates the total performance comprehensively and is closer to the practical scenarios of time-of-fly (ToF) applications.

Solid mechanics and electrostatics module are used in the pMUT device, and the mechanical damping and dielectric loss are set to 1/1000 and 1/100, respectively. The medium loss due to liquid viscosity is considerable in high-frequency pMUT, thus the thermoviscous acoustic module is adopted in the acoustic propagation medium, and the radiating boundary in the acoustic domain is used to absorb the radiated acoustic waves.

Fig. 2 (a) show the FEM model for transmitting sensitivity. The peripheral boundary of the loaded medium (water) is set as radiating boundary, and the peripheral area of solids is set to the perfectly matched layer (PML). The width and height of the water are set to 500 μm and 2 mm, respectively. The top

electrodes are alternately connected to $+1$ V/-1 V, while the bottom electrode is connected to the ground. The transmitting sensitivity S_{Tx} is defined as the absolute sound pressure at 2 mm above the center of pMUT divided by the excitation voltage (in the unit of [Pa/V]).

In the receiving model shown as Fig. 2 (b), the water is set to "Background pressure" boundary with 1 Pa pressure and "Wave direction" along (0, 0, -1). The receiving electrodes are terminated to a 1 MΩ resistor. The receiving sensitivity S_{Rx} is defined as the receiving voltage divided by the ground pressure (in the unit of [V/Pa]).

Fig. 2 (c) shows the schematic of the FEM model simulating pulse-echo response. The width and height of the water are set to 500 μm and 10 mm, respectively. The thermoviscous acoustic domain in the time domain is used. The excitation source is a Gaussian pulse voltage source in series with a 10 kΩ resistor. The Gaussian pulse is $\exp(-(t - 2T_0)^2/(T_0/2)^2)\sin(\omega_0 t)$. T_0 is the period corresponding to the resonant frequency f_0.

B. MODE SHAPE AND STRESS

Stress distribution guides optimal electrode design. To effectively excite the pMUT, the gap of the electrode circle should be aligned with the nodal point of the stress. The theoretical displacement and stress can be obtained by (1b) and $\nabla^2 \psi_{0n}$, respectively. The eigenmode study is employed in the FEM analysis, the stress is calculated from the Gauss point on the neutral axis. Fig. 3 (a) shows the theoretical and FEM simulated results of normalized displacement distribution of mode (0, 1) and mode (0, 3), while Fig. 3 (b) shows the normalized stress distribution. The slight discrepancy of displacement between theory and FEM is due to the difference between the FEM physical boundary and the theoretical clamped boundary. The normalized radius $\bar{r}$ of the stress nodal circle of FEM for mode (0, 1) and mode (0, 3) are located at $\bar{r} = \{0.686\}$ and $\{0.270, 0.596, 0.928\}$, respectively. The average error between the theoretical and FEM results is only 2.7%, and the performance variation is less than 2%. Thus, the radius of the theoretical stress nodal circle given in Table 1 is still instructive. The optimal
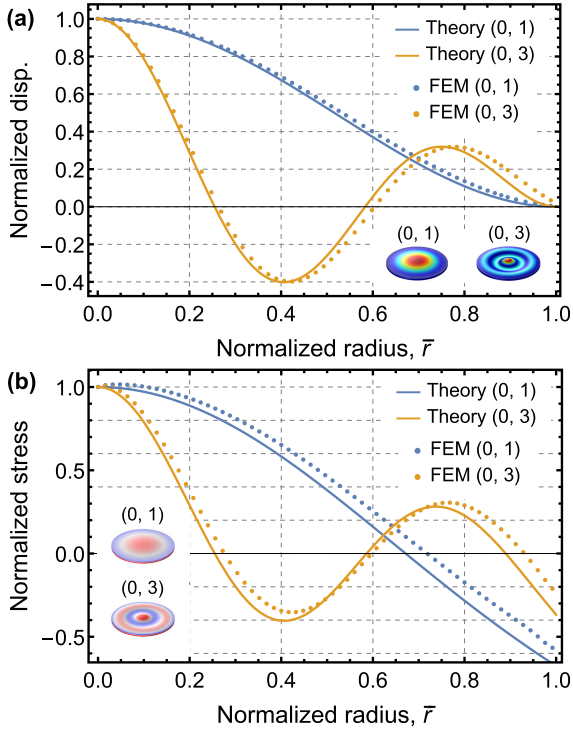
FIGURE 3. **(a) Normalized displacement and (b) Normalized stress distribution of mode (0, 1) and mode (0, 3) along radial. The continuous curves are theoretical results, while the dots represent FEM simulated results. The insets at the corner show the mock-up views of the displacement and stress distribution in FEM models while the substrate is hidden.**

FIGURE 4. **The FEM simulated frequency response of S_x in different mode vary with oxide layer thickness t_{ox}. The curves increase from purple to red, corresponding to t_{ox} increase from 0.25 to 5 μm with a step of 0.25 μm. (a) S_{Tx}, (c) S_{Rx} and (e) S_{RT} of (0, 1) mode pMUT; (b) S_{Tx}, (d) S_{Rx} and (f) S_{RT} of (0, 3) mode pMUT.**

FIGURE 5. **The simulated and theoretical performance metrics vary with the thickness of the oxide layer. (a) Resonant frequency f_0, (b) Static displacement A_s, (c) Normalized transmitting sensitivity bandwidth SBW_{Tx}, (d) Normalized Receiving sensitivity bandwidth SBW_{Rx}, and (e) Normalized round-trip sensitivity bandwidth SBW_{RT}. The SBWs are normalized to the maximum value of mode (0, 1).**

electrode corresponding to FEM results will be adopted in the following analysis.

C. THICKNESS

In ToF applications, the SBW_{RT} should be concerned. There are only two dimensions might affect SBW, i.e., radius a and stack layer thicknesses. They determine the resonant frequency f_0 and static displacement sensitivity A_s, and further influence the SBWs. Combine (3), (4), (8) and (17), noting that $f_0 \propto 1/a^2$ and $A_s \propto a^2$, then the SBW_{RT} that determined by the product of them should be independent of the radius a. The location of the neutral axis is dominated by the thickness of the piezoelectric and passive layers (t_p and t_{ox}). Since t_p is typically 0.5-1 μm while t_{ox} can vary in a wide range, the effect of t_{ox} on performance will be analyzed.

Figs. 4 (a)-(f) show the FEM simulated frequency responses of sensitivities in different modes vary with t_{ox}. Figs. 4 (a), (c), and (e) show transmitting sensitivity S_{Tx}, receiving sensitivity S_{Rx} and round-trip sensitivity S_{RT} of (0, 1) mode pMUT, respectively. While Figs. 4 (b), (d), and (f) show the corresponding performance of (0, 3) mode pMUT. pMUTs in both modes are excited by their optimize electrode configurations that have been discussed in Section III-B. The maximum S_{Tx} of (0, 3) mode is 12.5 times that of (0, 1) mode, which is a remarkable improvement in transmitting
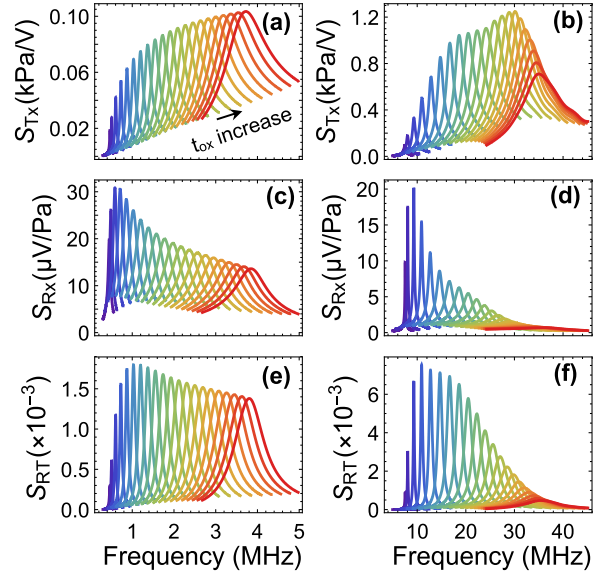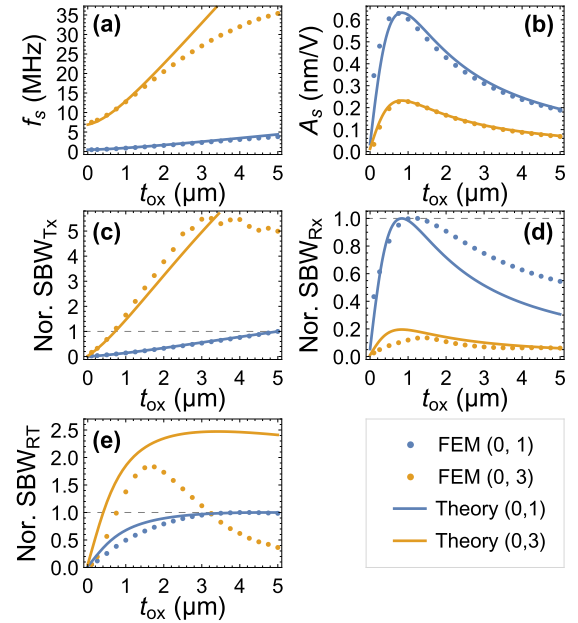
performance. However, S_{Rx} of (0, 3) mode is lower than (0, 1) mode, and there is a 30% reduction for maximum value. Finally, the S_{RT} of (0, 3) mode is 5.7 times that of (0, 1) mode.

TABLE 4. Summary of the performance in two pMUT designs.

Design	S_{Tx}(Pa/V)	S_{Rx}(μV/Pa)	$S_{RT}(10^{-3})$	$SBW_{RT}(10^{-3})$
(0, 1)	100.62	15.43	1.55	0.20
(0, 3)	1023.3	6.25	6.39	0.37

The improvement of S_{Tx} and reduction of S_{Rx} are predicted as (11) and (15).

Fig. 5 shows the major performance metrics vary with the thickness of oxide t_{ox}. Figs. 5 (a) and (b) show the dependency of resonant frequency f_0 and static displacement sensitivity A_s on t_{ox}. The relationship of f_0, A_s with t_{ox} will be discussed first. It can be estimated from (4) and (8), when t_{ox} is small enough, $t \approx t_p$, $z_p \approx 0$, thus $A_s \approx 0$ and f_s obtains a minimum value; when t_{ox} is high enough, $t \approx t_{ox}$, the flexural rigidity $D \propto t^3$, $z_p \approx t/2$, and $\mu \propto t_{ox}$, resulting in $A_s \propto 1/t_{ox}$ and $f_0 \propto t_{ox}$. As shown in Fig. 5 (a) and (b) that when $t_{ox} > 2$ μm A_s is negatively correlated with t_{ox} and f_0 is almost linear with t_{ox}. The clamped plate theory tends to overestimate f_0 of mode (0, 3) when $t_{ox} > 2$ μm, due to the assumption that $a \gg t$ made in the theory is no longer valid. It is worth mentioning that Fig. 5 (a) shows that there is an optimal value of t_{ox} for A_s around 0.8 μm.

Figs. 5 (c)-(e) show the effect of t_{ox} on the normalized SBWs, which are extracted from the sensitivity frequency responses in Fig. 4. The trend of normalized SBW_{Tx}, SBW_{Rx} and SBW_{Rx} with t_{ox} can be roughly estimated by (11), (15) and (17), respectively. SBWs eliminates the effect of Q-factors, thus Q is neglected in the following qualitative analysis. Equation (11) implies that $SBW_{Tx} \propto f_0^2 A_s$, which is monotonically increasing with total thickness, which is shown as Fig. 5 (c). Equation (15) shows that $SBW_{Rx} \propto A_s \alpha_{0n}$, thus the tendency of SBW_{Rx} in Fig. 5 (d) is similar with A_s in Fig. 5 (b).

Finally, SBW_{RT} is proportional to $(f_0 A_s)^2$, when t_{ox} is high enough, the SBW_{RT} should tend to be a constant. Fig. 5 (e) shows that at $t_{ox} = 1.75$ μm the simulated maximum SBW_{RT} of (0, 3) mode is 1.83. For (0, 1) mode, SBW_{RT} tends to be constant when t_{ox} exceeds 4 μm in theory, and the simulation shows that $t_{ox} = 4.25$ μm corresponds to maximum of SBW_{RT}. The simulated SBW_{RT} of (0, 1) is consistent well with theory, while that of (0, 3) mode declines rapidly and deviates from the theory curve after $t_{ox} = 1.75$ μm. On one hand, the clamped plate theory tends to overestimate f_0. On the other hand, the additional losses might come from the support loss ($Q_{support} \propto (a/t)^3$) and the thermal viscosity loss at a higher frequency. Thus, to obtain the corresponding maximum SBW_{RT}, $t_{ox} = 4.25$ μm is adopted as the optimal value for (0, 1) mode, while $t_{ox} = 1.75$ μm adopted for (0, 3) mode in the following analysis.

IV. RESULTS
A. FREQUENCY RESPONSE
Figs. 6 (a)-(c) show the frequency response of transmitting sensitivity S_{Tx}, receiving sensitivity S_{Tx} and round-trip
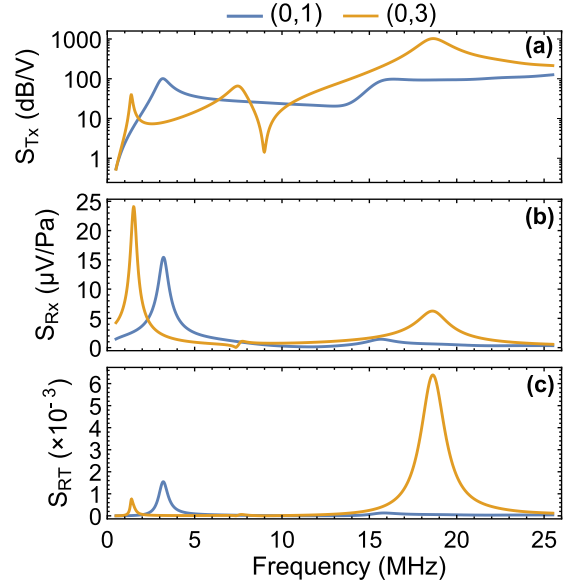

FIGURE 6. The simulated transmitting, receiving, and round-trip performance with different pMUT designs in the same radius a = 50 μm. (a) Transmitting sensitivity; (b) Receiving sensitivity; and (c) Round-trip sensitivity of the two pMUTs design that optimized for (0, 1) and (0, 3) mode.

sensitivity S_{RT} of two pMUT designs that optimized for (0, 1) and (0, 3) mode, which are labeled as (0, 1) and (0, 3), respectively. The S_{Tx} is shown in logarithms form, due to the gigantic difference between the two designs. Fig. 6 (a) shows that (0, 3) pMUT demonstrates extraordinary transmitting performance improvement compared to (0, 1) pMUT. The maximum S_{Tx} of (0, 3) pMUT is 10.2× of (0, 1). As shown in Fig. 6 (b), the receiving sensitivity of (0, 3) pMUT, however, is only 0.41× of (0, 1) pMUT. Fig. 6 (c) shows that maximum S_{RT} of (0, 3) pMUT is 4.12× of (0, 1) pMUT. Table 4 summarized the performance comparison of two pMUT designs. The SBW_{RT} of (0, 3) is about 1.85× of (0, 1) pMUT, which is consistent with Fig. 5 (e).

B. DIRECTIVITY
Fig. 7 shows the sound pressure level (SPL) spatial distribution of (0, 3) mode pMUT while (0, 1) mode as a reference when $a = 50$ μm and driving voltage is 1 V. The reference sound level in water is 1 μPa. In contact with water ($c_0 = 1481$ m/s), the f_0 of demonstrated (0, 1) and (0, 3) pMUTs are 3.18 MHz and 18.60 MHz, respectively. Fig. 7 (a) shows that (0, 3) mode exhibits not only higher SPL but also more concentrated field distribution, i.e., higher directivity. According to product theorem [14], the overall array directivity is the product of the element directivity and the array factor. Thus, with the same array form (array factor), higher element directivity results in higher overall array directivity.

The simulated and theoretical results of the normalized radiation pattern for the pressure of (0, 1) and (0, 3) pMUTs are shown in Fig. 7 (b). The (0, 1) pMUT almost produces
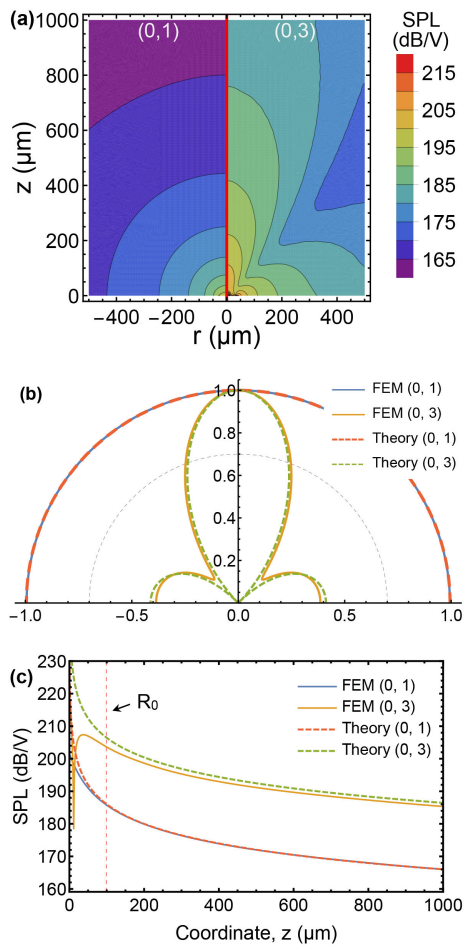
FIGURE 7. Spatial distribution and directivity of output SPL for (0, 3) mode pMUT, while traditional (0, 1) mode pMUT as comparing target. The pMUT (*a* = 50 µm) is located at cylindrical coordinates *z* = 0, *r* = 0. (a) Contour plot of output SPL. (b) Simulated and theoretical directivity. (c) Simulated and theoretical SPL along the *z*-axis.

the omnidirectional pattern, while (0, 3) demonstrates much better directivity. The theoretical half power beam width (HPBW) of (0, 3) is 38.9°, while simulated HPBW is 40.5°, producing a directivity of ∼5.0, which implies that with the same radiated power and distance, (0, 3) mode will produce about 5 times the sound pressure of the omnidirectional (0, 1) mode at the maximum radiation direction.

The simulated and theoretical SPL along the *z*-axis is shown in Fig. 7 (c). The Rayleigh distance R_0 of (0, 3) mode is 98.7 µm, while that of (0, 1) mode is 16.8 µm. In the far field ($z > R_0$), the pressure is nearly inversely proportional to distance. The SPL of (0, 3) mode is 20.38 dB higher than mode (0, 1), which is consistent with the previous 10.4× improvement in S_{Tx}. The simulated SPL of (0, 3) mode is slightly lower (0.3 dB) than the theoretical analysis, which is partially due to higher thermal viscous loss at a higher frequency.
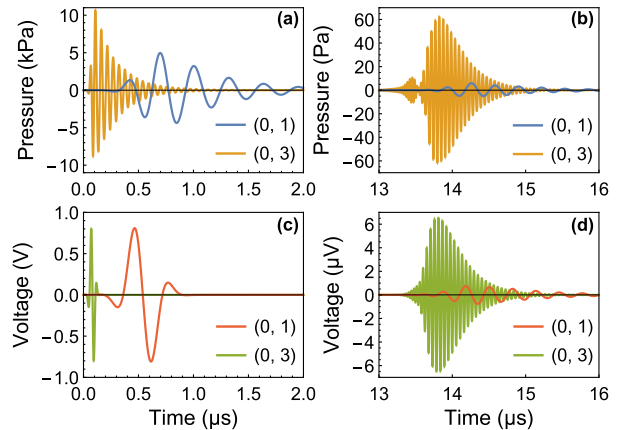
FIGURE 8. The simulated pulse-echo response of (0, 1) and (0, 3) mode pMUT designs with the same radius. (a) The transmitting surface pressure and (b) The receiving echo pressure at the center of the pMUTs surface. (c) The driving voltage. (d) The receiving voltage generated by the echo.

C. PULSE-ECHO RESPONSE

To compare the device on the same time scale, the height of the water is set to 10 mm, then the total round-trip time is about 13.5 µs. The radius of the (0, 3) and (0, 1) are both 50 µm to compare their efficiency with the same area. The detail of the pulse-echo simulation setting has been shown in Section III-A.

The proposed (0, 3) pMUT exhibits extraordinary round-trip performance compared with (0, 1) pMUT. The surface pressure (P_0) at the center of pMUTs is shown in Fig. 8 (a). Two pMUT designs are driven by the voltage shown in Fig. 8 (c), which is the product of the Gaussian function and the sine function. The (0, 3) pMUT generates a surface pressure of 10.6 kPa, which is 2.15× of (0, 1) pMUT (4.96 kPa). The echo pressure is reflected by the hard boundary and then returns to the surface of pMUTs are shown in Fig. 8 (b). After reflected by the hard boundary, the echo pressure of (0, 3) pMUT (62.0 Pa) is 10.5× of (0, 1) pMUT (5.88 Pa), which is consistent with the improvement of S_{Tx} (10.2×).

The receiving voltage of pMUTs is shown in 8 (d). In the reception, the maximum receiving voltage of (0, 3) pMUT is 6.53 µV, which is 8.6× of (0, 1) pMUT (0.76 µV). The ratio of receiving voltage between the two designs is higher than the ratio of S_{RT} (4.12×), due to the mismatch between terminal resistance and the pMUT reactance. The capacitance of (0, 1) and (0, 3) pMUT are 0.368 and 0.140 pF, which correspond to the reactance of 136 and 61 kΩ, leads to an output voltage ratio of 2.05. Thus, the maximum receiving voltage ratio is about 4.12 × 2.05≈8.5.

V. CONCLUSION AND DISCUSSION

This work proposed the pMUT designs with high-order axisymmetric mode. To prove the concept, 3rd-order mode is used for the analysis, while traditional 1st-order axisymmetric mode as a reference. Analytical models for nth-order

axisymmetric modes are provided for the performance analysis of resonant frequency f_0, displacement sensitivity A_s, transmitting sensitivity S_{Tx}, receive sensitivity S_{Rx}, round-trip sensitivity S_{RT} and directivity, which gives guidance for optimization of high-order pMUTs and are verified by FEM simulation. Through optimization of electrode configuration, and layer thickness, the proposed (0, 3) pMUT demonstrates significant performance improvement compared with conventional (0, 1) pMUT designs in terms of transmitting, round-trip performance, and high directivity. These features make high-order mode pMUTs very promising for forming high-frequency large-scale arrays.

Conventional phased array typically required a half wavelength distance limit to suppress the sidelobe. However, (0, 3) pMUT has a minimum cell distance (100 µm) that is more than a wavelength (80 µm). The Fermat's spiral arrays [23] with sparse array forms help to break this limitation. A focused, narrow acoustic beam is essential for high-resolution and pulse-echo ultrasound imaging [24]. The high directivity of high-order modes is conducive to generate a focused beam without beam forming technique but reduces the angle in reception. Therefore, the combination design that contains high-order mode pMUTs with high-transmitting performance and high directivity and 1st-order pMUTs with high-receiving performance and entropy might be more favorable to pMUT arrays for applications of object detection and medical imaging.
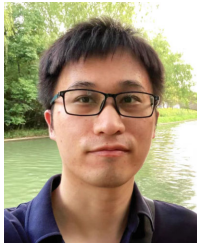
REFERENCES

[1] D. E. Dausch, K. H. Gilchrist, J. B. Carlson, S. D. Hall, J. B. Castellucci, and O. T. von Ramm, "In vivo real-time 3-D intracardiac echo using PMUT arrays," *IEEE Trans. Ultrason., Ferroelectr., Freq. Control*, vol. 61, no. 10, pp. 1754–1764, Oct. 2014.

[2] Y. Lu, A. Heidari, and D. A. Horsley, "A high fill-factor annular array of high frequency piezoelectric micromachined ultrasonic transducers," *J. Microelectromech. Syst.*, vol. 24, no. 4, pp. 904–913, Aug. 2015.

[3] Y. Lu and D. A. Horsley, "Modeling, fabrication, and characterization of piezoelectric micromachined ultrasonic transducer arrays based on cavity SOI wafers," *J. Microelectromech. Syst.*, vol. 24, no. 4, pp. 1142–1149, Aug. 2015.

[4] S. Akhbari, F. Sammoura, B. Eovino, C. Yang, and L. Lin, "Bimorph piezoelectric micromachined ultrasonic transducers," *J. Microelectromech. Syst.*, vol. 25, no. 2, pp. 326–336, Apr. 2016.

[5] S. Akhbari, F. Sammoura, and L. Lin, "Equivalent circuit models for large arrays of curved and flat piezoelectric micromachined ultrasonic transducers," *IEEE Trans. Ultrason., Ferroelectr., Freq. Control*, vol. 63, no. 3, pp. 432–447, Mar. 2016.

[6] T. Xu et al., "Equivalent circuit models of cell and array for resonant cavity-based piezoelectric micromachined ultrasonic transducer," *IEEE Trans. Ultrason., Ferroelectr., Freq. Control*, vol. 67, no. 10, pp. 2103–2118, Oct. 2020.

[7] K. Smyth, S. Bathurst, F. Sammoura, and S.-G. Kim, "Analytic solution for N-electrode actuated piezoelectric disk with application to piezoelectric micromachined ultrasonic transducers," *IEEE Trans. Ultrason., Ferroelectr., Freq. Control*, vol. 60, no. 8, pp. 1756–1767, Aug. 2013.

[8] K. Smyth and S.-G. Kim, "Experiment and simulation validated analytical equivalent circuit model for piezoelectric micromachined ultrasonic transducers," *IEEE Trans. Ultrason., Ferroelectr., Freq. Control*, vol. 62, no. 4, pp. 744–765, Apr. 2015.

[9] A. W. Leissa, *Vibration of Plates*, document NASA-SP-160, U.S. Government Printing Office, Washington, DC, USA, Jan. 1969.

[10] G.-L. Luo, Y. Kusano, and D. A. Horsley, "Airborne piezoelectric micromachined ultrasonic transducers for long-range detection," *J. Microelectromech. Syst.*, vol. 30, no. 1, pp. 81–89, Feb. 2021.

[11] D. Horsley, Y. Lu, and O. Rozen, "Flexural piezoelectric resonators," in *Piezoelectric MEMS Resonators* (Microsystems and Nanosystems), H. Bhugra and G. Piazza, Eds. Cham, Switzerland: Springer, 2017, pp. 153–173.

[12] H. Lamb, "On the vibrations of an elastic plate in contact with water," *Proc. Royal Soc. London. Ser. A*, vol. 98, no. 690, pp. 205–216, Nov. 1920.

[13] M. Amabili and M. K. Kwak, "Free vibrations of circular plates coupled with liquids: Revising the Lamb problem," *J. Fluids Struct.*, vol. 10, no. 7, pp. 743–761, Oct. 1996.

[14] D. T. Blackstock, "Fundamentals of physical acoustics," *Acoust. Soc. Amer.*, vol. 109, no. 4, pp. 1274–1276, 2001.

[15] M.-A. Dubois and P. Muralt, "PZT thin film actuated elastic fin micromotor," *IEEE Trans. Ultrason., Ferroelectr., Freq. Control*, vol. 45, no. 5, pp. 1169–1177, Sep. 1998.

[16] P. Muralt, A. Kholkin, M. Kohli, and T. Maeder, "Piezoelectric actuation of PZT thin-film diaphragms at static and resonant conditions," *Sens. Actuators A, Phys.*, vol. 53, nos. 1–3, pp. 398–404, May 1996.

[17] P. Muralt et al., "Piezoelectric micromachined ultrasonic transducers based on PZT thin films," *IEEE Trans. Ultrason., Ferroelectr., Freq. Control*, vol. 52, no. 12, pp. 2276–2288, Dec. 2005.

[18] Y. Kozlovsky, "Vibration of plates in contact with viscous fluid: Extension of Lamb's model," *J. Sound Vibrat.*, vol. 326, nos. 1–2, pp. 332–339, Sep. 2009.

[19] K. K. Park, H. J. Lee, P. Crisman, M. Kupnik, O. Oralkan, and B. T. Khuri-Yakub, "Optimum design of circular CMUT membranes for high quality factor in air," in *Proc. IEEE Ultrason. Symp.*, Nov. 2008, pp. 504–507.

[20] Q. Wang, Y. Lu, S. Mishin, Y. Oshmyansky, and D. A. Horsley, "Design, fabrication, and characterization of scandium aluminum nitride-based piezoelectric micromachined ultrasonic transducers," *J. Microelectromech. Syst.*, vol. 26, no. 5, pp. 1132–1139, Oct. 2017.

[21] Y. Kusano, I. Ishii, T. Kamiya, A. Teshigahara, G.-L. Luo, and D. A. Horsley, "High-SPL air-coupled piezoelectric micromachined ultrasonic transducers based on 36% ScAlN thin-film," *IEEE Trans. Ultrason., Ferroelectr., Freq. Control*, vol. 66, no. 9, pp. 1488–1496, Sep. 2019.

[22] L.-M. He, W.-J. Xu, Y. Wang, J. Zhou, and J.-Y. Ren, "Sensitivity—bandwidth optimization of PMUT with acoustical matching using finite element method," *Sensors*, vol. 22, no. 6, p. 2307, Mar. 2022.

[23] O. Martínez-Graullera, C. J. Martín, G. Godoy, and L. G. Ullate, "2D array design based on Fermat spiral for ultrasound imaging," *Ultrasonics*, vol. 50, no. 2, pp. 280–289, Feb. 2010.

[24] Y. Lu, H.-Y. Tang, S. Fung, B. E. Boser, and D. A. Horsley, "Short-range and high-resolution ultrasound imaging using an 8 MHz aluminum nitride PMUT array," in *Proc. 28th IEEE Int. Conf. Micro Electro Mech. Syst. (MEMS)*, Jan. 2015, pp. 140–143.

KANGFU LIU (Student Member, IEEE) received the B.S. degree in microelectronic engineering from Xidian University, Xi'an, China, in 2018, and the Ph.D. degree in microelectronics and solid state physics from the Shanghai Institute of Microsystem and Information Technology (SIMIT), Shanghai, China, in 2023. His research interests include the design and theory techniques of piezoelectric RF resonators and filters, and MEMS-based piezoelectric transducers and applications.

YAOQING LU (Student Member, IEEE) received the B.S. degree from the Southwest University of Science and Technology, Mianyang, China, in 2020, and the M.S. degree from ShanghaiTech University, Shanghai, China, in 2023. Her research interests include MEMS transducers and applications.

SHENG WU (Student Member, IEEE) received the B.S. degree in microelectronic engineering from the Hefei University of Technology, Hefei, China, in 2018, and the Ph.D. degree in microelectronics and solid state physics from the Shanghai Institute of Microsystem and Information Technology (SIMIT), Shanghai, China, in 2023. His research interests include the design and fabrication techniques of piezoelectric micromachined ultrasonic transducer, and MEMS-based piezoelectric transducers and applications.

XINXIN LI received the B.S. degree in semiconductor physics and devices from Tsinghua University, Beijing, China, in 1987, and the Ph.D. degree in microelectronics from Fudan University, Shanghai, China, in 1998. He was a Research Engineer with the Shenyang Institute of Instrumentation Technology, Shenyang, China, for five years, a Research Associate with The Hong Kong University of Science and Technology, Hong Kong, and a Research Fellow with Nanyang Technological University, Singapore. He then joined with Tohoku University, Sendai, Japan, as a Lecturer (Center of Excellence Research Fellowship). Since 2001, he has been a Professor with the Shanghai Institute of Microsystem and Information Technology, Chinese Academy of Sciences, Shanghai. Since 2007, he has been the Director with the State Key Laboratory of Transducer Technology, Shanghai. He has published more than 300 papers in refereed journals and conference proceedings (including about 160 SCI papers) and holds more than 80 patents. For a long time, his research interests have been in micro/nanosensors and micro/nano-electro-mechanical-systems. He served as the Technical Program Committee Member for the IEEE Micro Electromechanical Systems (MEMS) Conference in 2008, 2011, and 2017, and the IEEE Sensors Conference from 2002 to 2014. Since 2014, he has been serving as an International Steering Committee Member for the Conference on Solid-State Sensors, Actuators and Microsystems (Transducers). He is currently on the Editorial Board of the *Journal of Micromechanics and Microengineering*.
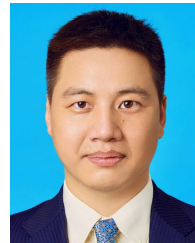
TAO WU (Senior Member, IEEE) received the Ph.D. degree from the University of California at Los Angeles, Los Angeles, CA, USA, in 2011. From 2014 to 2015, he was with Intel Corporation, Hillsboro, OR, USA. From 2014 to 2017, he was a Post-Doctoral Research Fellow with Stanford University, Stanford, CA, USA, and Northeastern University. He is currently an Assistant Professor with the School of Information Science and Technology, ShanghaiTech University, Shanghai, China. He has authored or coauthored more than 100 papers in prestigious journals and conferences. His research interests include design and fabrication of multiferroic transducers, piezoelectric resonators, and integrated circuit for MEMS-based microsystems.

● ● ●